

FEDSM-ICNMM2010-30190

DRAG REDUCTION OF FILAMENTS AND POROELASTIC BODIES BY NON-LINEAR DEFORMATION

Frédéric P. Gosselin

Laboratoire de Nanorobotique
École Polytechnique de Montréal
Montréal, Québec, H3T 1J4, Canada
Email: frederick.gosselin@polymtl.ca

Emmanuel de Langre*

Département de Mécanique
Ladhyx-CNRS
École Polytechnique
Palaiseau, 91128, France
Email: delangre@ladhyx.polytechnique.fr

ABSTRACT

Because of their flexibility, trees and other plants deform with great amplitude (reconfigure) when subjected to fluid flow. Hence the drag they encounter does not grow with the square of the flow velocity as it would on a classical bluff body, but rather in a less pronounced way. The reconfiguration of actual plants has been studied abundantly in wind tunnels and hydraulic canals, and recently a theoretical understanding of reconfiguration has been brought by combining modelling and experimentation on simple systems such as filaments and flat plates. These simple systems have a significant difference with actual plants in the fact that they are not porous: fluid only flows around them, not through them. We present experimentation and modelling of the reconfiguration of a simple poroelastic system. Proper scaling of the drag and the fluid loading allows comparing the reconfiguration regimes of porous systems to those of simple systems. It is found that in the large reconfiguration regime, the scaling of the drag with flow velocity is independent of the porosity for a range of parameter values.

INTRODUCTION

In most traditional engineering applications, structures are designed to be rigid such that the loads they bear do not deform them substantially. In nature, the opposite is true [1]; especially for trees and plants whose largest abiotic stresses are

aero/hydrodynamic fluid loadings [2]. Plants are flexible where man-made structures are stiff. The great flexibility of plants comes as the solution to an optimization problem plants face: that of maximizing surface area and height to capture sunlight with a finite quantity of material [3]. It is essential to understand the fluid loadings on plants in order to devise better models to comprehend and predict wind damages to forests and crops, as well as to study the adaptation of aquatic and terrestrial plants to their environment.

Trees and other plants deform with great amplitude when subjected to fluid flow like wind or water current. We term this global change of shape *reconfiguration* [3]. By bending and twisting under fluid loading, plants reconfigure and the drag they encounter does not grow with the square of the flow velocity as it would on a classical bluff body, but rather in a less pronounced way. We express in a simplified way this modification of the dependence on velocity of the drag by the Vogel exponent \mathcal{V} [1, 3], such that

$$F \propto U_{\infty}^{2+\mathcal{V}}, \quad (1)$$

where F is the drag force and U_{∞} is the flow velocity. For example, the leaf of the tulip tree rolls up into a cone when subjected to increasing wind speed [4] hence decreasing its cross-sectional area and becoming more streamlined. This reconfiguration has for effect that the drag on the leaf increases more or less linearly with flow speed ($\mathcal{V} \sim -1$). The reconfigurations of many species

*Address all correspondence to this author.

of plants have been studied in wind tunnels, tow tanks and hydraulic canals. Collections of measures of reconfiguration and Vogel exponents for various species can be found in Vogel [1, p. 143] as well as Harder et al. [5].

Recently a more fundamental understanding of the mechanisms of reconfiguration has been brought by combining modelling and experimentation on simple systems such as filaments and flat plates [6–10]. Alben et al. [6] studied the reconfiguration of a flexible filament supported at its centre in a 2D soap film flow. The drag reduction and the bending deformation of the filament measured experimentally were properly modelled with a potential flow theory coupled with a Euler-Bernoulli beam formulation. From their experimental and theoretical results, Alben et al. [6] concluded that the scaling of the drag of the fibre transitioned from a rigid regime ($\mathcal{V} = 0$) to a large deformation regime with $\mathcal{V} = -2/3$ as the hydrodynamic force was increased with respect to the rigidity of the fibre.

Gosselin et al. [10] compared drag measurements of flexible thin plates in a wind tunnel with predictions from a simplified model based on an empirical drag formulation. The simplified model predicts well the reconfiguration of plates and further comparisons showed that the reconfiguration of a rectangular flexible plate supported at its centre in a wind tunnel is identical to that of a filament in a soap film as studied by Alben et al. [6]. Moreover, Gosselin et al. showed that in the regime of large deformation, the scaling of the drag with the flow velocity can be deduced by dimensional analysis through the assumption that as the deformation is large, the original characteristic length becomes irrelevant.

The study of the reconfiguration of idealised systems [6–10] allowed understanding the basic mechanisms of drag reduction affecting trees and vegetation. However, a major difference separates beams and plates from actual trees: fluid must flow *around* simple obstacles while wind passes *through* a porous structure such as a tree. The elements composing the plants like the leaves and the branches perceive an effective flow velocity modified from that of the free stream velocity. Because the plant is a poroelastic system, when reconfiguring, it modifies this effective flow velocity. It is the goal of the present paper to characterise the effect on reconfiguration of poroelasticity. Extensive wind tunnel testing was realised on poroelastic bodies as well as flexible filaments. These experimental results allow us to define a proper Cauchy number which governs the problem of reconfiguration and accounts for geometry, Reynolds and porosity effects. Moreover, with a simple theoretical model for the reconfiguration of the systems studied, we investigate the mechanisms of drag reduction and study the effect of porosity on reconfiguration.

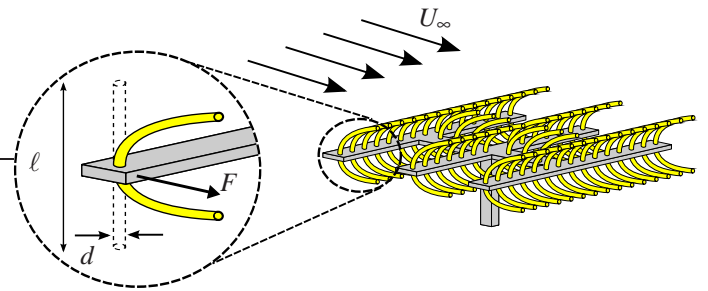


FIGURE 1: Schematic diagram of the support holding 50 identical filaments and details of one filament.

EXPERIMENTS

To understand the effect of porosity on the problem of reconfiguration, we performed experiments in a wind tunnel to measure the drag of simple filaments as well as that of poroelastic bodies.

Methodology

We measured the drag of flexible cylindrical filaments of diameter d , length ℓ and flexural rigidity B (figure 1). Three specimens of filaments supported at their centre were tested, their properties are given in table 1. Because the filaments were small and had little drag, 50 identical filaments were mounted on a specially designed support to test them in the wind tunnel (figure 2). A significant measure of drag could thus be obtained. The spacing between the filaments on the support was of 10 diameters in the transverse direction and 40 diameters in the streamwise direction. The interaction between filaments is thus neglected. To avoid a bidimensional deformation, the filaments were mounted vertically in the wind tunnel. Hence, the lower half of a filament is rigidified by gravity and the upper half is effectively more flexible. At first order, on the whole filament, the effects of gravity is compensated and at high flow velocity, aerodynamic loading becomes much larger than weight. In addition, rigid cylinders of the same dimensions as the three flexible filaments were tested.

The poroelastic system studied is a ball of diameter D made of N round filaments of diameter d tied together at the center of the ball (figure 3). The core of the ball where all the filaments are tied is relatively rigid and has a diameter D_i . The ball is screwed onto a downstream support which transmits the drag force to the force sensor. The specimens were manufactured by Hasbro and sold as toys under the name of “Koosh balls”. The flexural rigidity B of the filaments forming the ball was found by measuring the natural frequency of a single cantilever filament using a high-speed camera. Two poroelastic specimens were tested in the wind tunnel, their characteristics are given in table 2. Moreover, a rigid porous specimen built with finishing nails planted in a styrofoam ball was tested (figure 4).

These laboratory experiments were conducted in a small Eif-

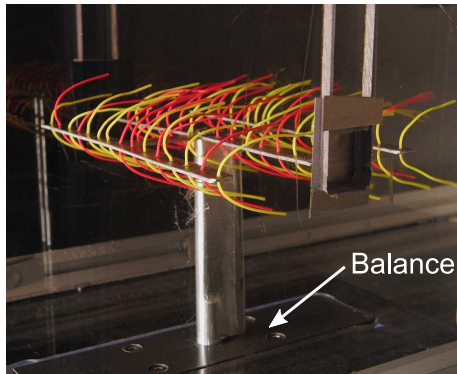


FIGURE 2: Photograph of the support holding 50 filaments of length $\ell = 7.4$ cm subjected to an air flow of 20 m/s.

	ℓ (cm)	d (cm)	B (10^{-6} Nm)
f1	4.0	0.094	127
f2	7.4	0.094	127
f3	11.6	0.094	127
c1	4.0	0.094	-
c2	7.4	0.094	-
c3	11.6	0.094	-

TABLE 1: Parameter values of the tested flexible filaments and rigid cylinders.

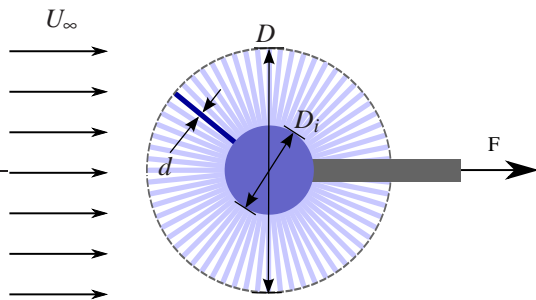


FIGURE 3: Schematic of the poroelastic system.

	D (cm)	D_i (cm)	d (cm)	B (10^{-6} Nm)	N
FP1	8.9	3.1	0.094	127	900
FP2	5.4	1.6	0.068	38.1	1150
RP	8.9	3.0	0.09	-	530

TABLE 2: Parameter values of the tested flexible and rigid porous specimens.

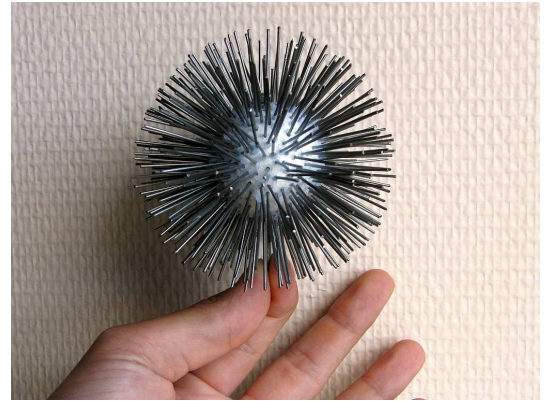


FIGURE 4: Photograph of the rigid porous specimen. It has the same dimensions as the first poroelastic specimen, but is made of less cylinders ($N = 530$).

fel wind tunnel with a test section of 0.180m by 0.180m. The wind stream is produced by a centrifugal fan mounted downstream and exhausting air vertically. The mean velocity in the test section can be varied from 5 to 30m/s with a turbulence level of 1.5% at 10m/s.

Different specimens tested were mounted on a support connected to a five-axis force sensor located under the wind tunnel. The force sensor measured the drag of the specimen and a pitot-static system measured the flow velocity. For every specimen at each flow velocity tested, the 24 bit data acquisition system collected the measurements of the drag and the flow velocity for one minute and time-averaged the values. The drag on the support alone was measured and subtracted from the drag of each specimen.

Reconfiguration and drag measurements

The deformation of the first poroelastic specimen (FP1) is shown in figure 5 for four flow velocities. At 5m/s (figure 5 a), the deformation is small. As the flow velocity is increased further, the deformation becomes important and the filaments bend with the flow. Note that on figure 5 (c), a dynamic coherent movement of the filaments makes the picture blurred. We presume that these coherent movements are due to a passive response of the filaments to vortex shedding on the ball. At 14m/s, the standard deviation of the fluctuations of the drag measurements is less than 8% of the time-averaged value. For this reason, in this study of static reconfiguration, we neglect any dynamic effect due to vortex shedding, turbulence or other coupling mechanisms.

The drag measurements of the filaments and the rigid cylinders are shown on figure 6 (a) while those for the three porous specimens are shown on figure 6 (b). For both the cylinders and the porous systems, the increase of drag with flow velocity on

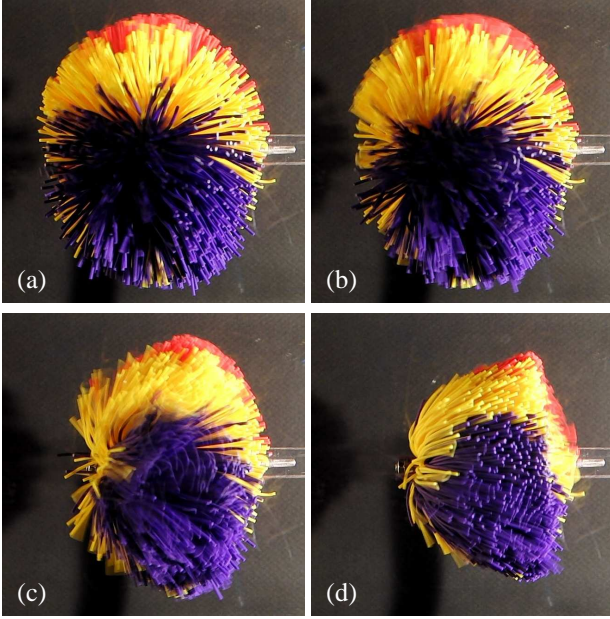


FIGURE 5: Photographs of the deformation of the first poroelastic specimen in the wind tunnel at flow velocities of 5 (a); 8 (b); 14 (c); and 29 m/s (d).

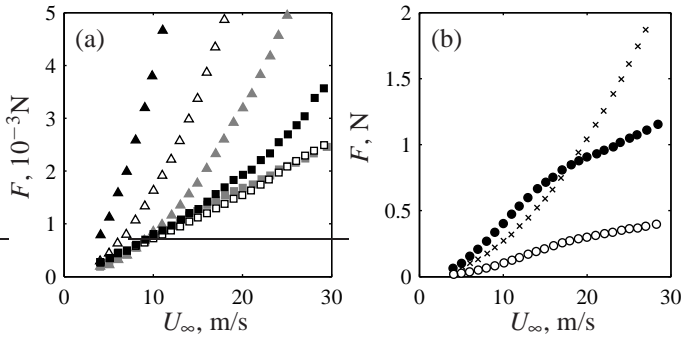


FIGURE 6: Drag of flexible filaments and rigid cylinders (a), as well as porous specimens (b): f1 (■); c1 (▲); f2 (□); c2 (△); f3 (■); c3 (▲); FP1 (●); FP2 (○); RP (×).

the rigid specimens is almost quadratic. However, the drag of all flexible specimens has a smaller dependence on the flow velocity.

To analyse the effect of flexibility on drag, we must first characterise the drag of the rigid benchmark specimens. We define a drag coefficient and a Reynolds number for the rigid cylinders $C_D = 2F/\rho d \ell U_\infty^2$ and $Re = \rho d U_\infty/\mu$ where F is the measured drag force, U_∞ is the flow velocity and ρ and μ are the fluid density and dynamic viscosity. Similarly for the rigid porous specimen, we define a drag coefficient $C_D = 8F/\pi \rho D^2 U_\infty^2$ and

use the same definition of Reynolds number based on the diameter of a cylinder of the porous ball. Due to the lack of space, the variations of drag coefficients with Reynolds number for the rigid cylinders and the rigid porous balls are not shown. Overall, it found that in the range of Reynolds number studied here varying between 200 and 2000, the drag coefficient of the porous ball follows a similar trend to that of the isolated rigid cylinders.

Using the data of the rigid benchmark specimens in figure 6, we can thus isolate the effect of flexibility on the drag variation of the flexible specimens as the flow velocity is varied. To extract from the drag measurements the variations due to flexibility and thus fully appreciate the effect of reconfiguration, we develop appropriate dimensionless numbers.

Dimensionless numbers

We consider the drag F of a flexible slender cylindrical filament of length ℓ , diameter d and flexural rigidity B bending due to a fluid flow of density ρ and velocity U_∞ . We express this problem using the Cauchy number and the reconfiguration number:

$$\widetilde{C}_Y = C_D \frac{\rho \ell^3 U_\infty^2 d}{16B}, \quad \mathcal{R} = \frac{F}{\frac{1}{2} \rho C_D \ell d U_\infty^2}. \quad (2)$$

The Cauchy number characterises the reconfiguration of an elastic medium subjected to flow [10–13]. It is equal to the ratio of the aerodynamic force produced by the fluid on the original shape of the structure over the rigidity of the structure. We use the definition introduced by Gosselin et al. [10] which includes the drag coefficient. This allows to take into account effects of geometry and Reynolds number. The reconfiguration number \mathcal{R} emphasises the effect of flexibility on the drag by comparing the drag of the flexible filament to that of an equivalent rigid cylinder at the same Reynolds number.

For the poroelastic system, similar Cauchy and reconfiguration numbers can be defined based on the cross-sectional area of the ball, and a new quantity, the surface density, is introduced

$$\widetilde{C}_Y = C_D \frac{\rho (D - D_i)^3 U_\infty^2 d}{16B}, \quad \mathcal{R} = \frac{8F}{\rho \pi D^2 C_D U_\infty^2}, \quad (3)$$

$$\eta = \frac{Nd \frac{D}{2}}{\frac{1}{4} \pi D^2} = \frac{2Nd}{\pi D}.$$

We define the surface density as the ratio of the cross-sectional area of all the components of the porous body (the N filaments composing the ball) over the cross-sectional area of the undeformed poroelastic body.

The variation of \mathcal{R} in function of \widetilde{C}_Y is shown in figure 7 for the three specimens of filaments (□). The new experimental

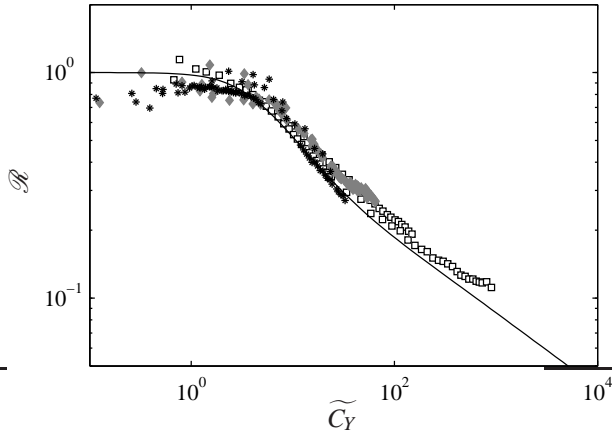


FIGURE 7: Superposition of the experimental measurements of drag on flexible slender systems: 3 flexible filaments tested in a wind tunnel (\square); 5 rectangular plates tested in a wind tunnel by [10] (*); and 2 fibres tested in a soap film flow by [6] (\blacklozenge); the theoretical model of [10] (—).

points are shown along with the results of Gosselin et al. [10] on flexible rectangular plates (*) and those of Alben et al. [6] on flexible fibres in a soap film flow (\blacklozenge). Despite the different geometries, dimensions, rigidity and type of flow, all the data points collapse on a single curve. This confirms that the problems of reconfiguration of a filament and a rectangular plate in a wind tunnel, as well as a fibre in a soap film flow are essentially the same problem, i.e., the same dimensionless numbers characterise them and their reconfiguration is the same. Note that superposition is only possible with the use of the Cauchy number definition of equation 2 which includes the drag coefficient C_D . Values of C_D for the different specimens plotted in figure 7 vary from 0.7 for the shortest filaments at the highest Reynolds number to 7 for the fibres in the soap film flow. The inclusion of the drag coefficient in the Cauchy number allows to fully isolate effects of flexibility on the drag from Reynolds number and geometry effects. For the sake of comparison, the reconfiguration curve predicted by the model of Gosselin et al. [10] which couples an empirical drag formulation to the large deformation of a Euler-Bernoulli beam is shown in solid line in figure 7. The agreement between the experiments and the model is very good, and for this reason, the model is extended to poroelastic systems in the following section.

The Cauchy number governs the problem of the reconfiguration of slender systems (figure 7). For small values of \widetilde{C}_Y , the points are aligned on a horizontal line which indicates that the drag on the flexible objects varies as it would on a rigid object. At values of \widetilde{C}_Y between 1 and 10, the reconfiguration number starts to decline as the specimens deform. As \widetilde{C}_Y increases further, the decline of \mathcal{R} seems to follow a constant logarithmic

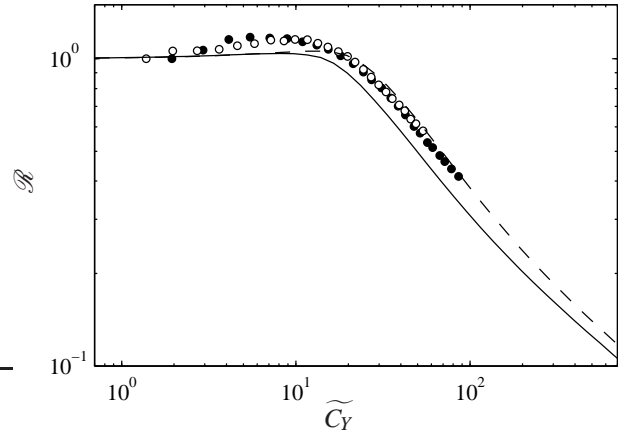


FIGURE 8: Variation of the drag reduction of the poroelastic systems for increasing Cauchy number: first flexible specimen, (\bullet); second flexible specimen, (\circ). The curves predicted by the theoretical model of equations 13-15 with $\eta = 6.1$ and 9.2 corresponding respectively to the first (—) and second (---) specimens are also shown.

slope. Upon fitting a least square power law on the data points of figure 7 where $\widetilde{C}_Y > 100$, one finds that $\mathcal{R} \propto \widetilde{C}_Y^{-0.29}$ which corresponds to $F \propto U_\infty^{1.42}$ or $\mathcal{V} = -0.58$. This value of Vogel exponent is in agreement with the dimensional analysis of Gosselin et al. [10] which predicts a Vogel exponent of $\mathcal{V} = -2/3$. Gosselin et al. obtain this value by dimensional analysis following the assumption that the characteristic length of the original undeformed system becomes irrelevant.

The reconfiguration curves for the first (\bullet) and the second (\circ) flexible specimens are shown on figure 8. The two curves are superimposed indicating that the Cauchy number is appropriate to describe the problem.

Differently from the reconfiguration of slender bodies in figure 7, the reconfiguration number of the poroelastic balls in figure 8 increases slightly before decreasing. At $\widetilde{C}_Y \approx 10$, the drag of the poroelastic balls is 18% larger than that of identical rigid porous balls. This can be explained by the fact that the filaments which point upstream in the flow before the ball is deformed must pass through a position where they are perpendicular to the flow to bend downstream with the flow (see figure 5 b-c), thus significantly increasing their drag. Some tree branches have been observed to exhibit the same phenomenon [3].

Another noticeable difference between figures 7 and 8, is that the drag reduction begins about $\widetilde{C}_Y \approx 3$ for the plates, fibres and filaments while \mathcal{R} only starts to decrease beyond $\widetilde{C}_Y \approx 20$ for the porous systems. The reconfiguration curve for the porous systems is shifted to higher values of \widetilde{C}_Y . This difference is highlighted in figure 9 (a) where \mathcal{R} is plotted for the slender specimens (\bullet) along with the poroelastic specimens (\bullet) versus the

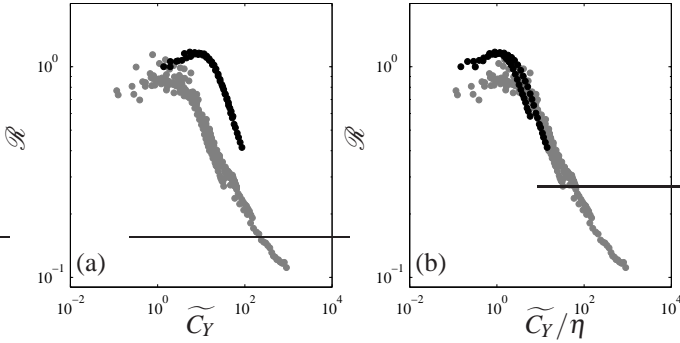


FIGURE 9: Collapse of the reconfiguration curves of porous (●) specimens as well as the slender specimens (filaments, rectangular plates, fibres, ●) when plotted in function of: the Cauchy number alone \widetilde{C}_Y , (a); the Cauchy number divided by the surface density \widetilde{C}_Y/η , (b).

Cauchy number. In figure 9 (b), the reconfiguration of both types of systems is plotted in function of the quotient of the Cauchy number by the surface density \widetilde{C}_Y/η . For the slender specimens, $\eta = 1$ while for the first and second poroelastic specimens it can be calculated from equation 3 with the data from table 2 to be respectively $\eta = 6.1$ and $\eta = 9.2$. Dividing the Cauchy number by the surface density amounts to dividing the aerodynamic load evenly on all the structural elements composing the porous bodies. By doing so, we obtain a reasonable collapse of reconfiguration points for both porous and non-porous bodies with a drag reduction which begins at \widetilde{C}_Y/η valued between 1 and 3. It is shown with the following theoretical model that this collapse can be extended on a much greater scale of surface density values.

THEORETICAL MODEL

We consider the deformation of a ball made up of a collection of N identical cylindrical beams uniformly spread and clamped at the centre of the ball (figure 10 a). The beams have rigidity per unit width B , diameter d length $D/2$ and form a ball of diameter D . This system is subjected to a flow of uniform velocity U_∞ of an inviscid fluid of density ρ .

The schematic diagram of a beam j part of the system along with the flow it perceives are shown in figure 10 (b). The undeformed beam j makes an angle Θ_j with the flow and has an azimuthal angle φ_j about the axis of the flow (figure 10 a). The lagrangian coordinate S_j is defined along the central axis of this beam from its clamped end to its free end. The deformed shape of beam j is given by the local angle $\theta_j(S_j)$ the beam makes with the flow.

We use an empirical formulation of the fluid forces based on the model of Gosselin et al. [10]. As in Gosselin et al. [10] and

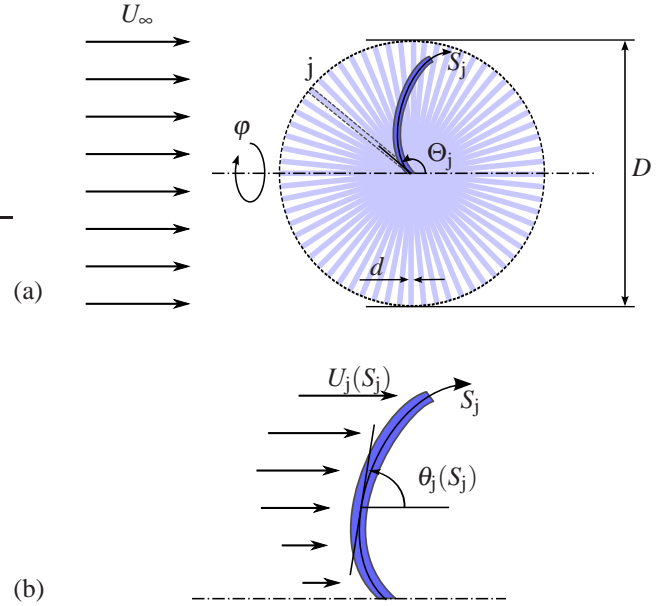


FIGURE 10: Schematic diagram of the poroelastic system modelled (a). Detail of the deformation of beam j part of the system along with the flow the beam perceives (b).

similarly to Taylor's [14] modelling of the drag force on yawed cylinders, we approximate the pressure drag on a beam in a potential flow with a conservation of momentum argument. We assume that the flow produces a force proportional to the momentum it carries in the direction perpendicular to the beam. Upon setting this drag force on a beam element equal to the shear force in a Euler-Bernoulli beam, we obtain:

$$B \frac{\partial^3 \theta_j}{\partial S_j^3} = -\frac{1}{2} \rho C'_D [U_j(S_j) \sin \theta_j]^2, \quad (4)$$

where C'_D is the drag coefficient of one beam inside the porous ball and where the velocity $U_j(S_j)$ perceived by beam j varies along the beam (figure 10 b). We neglect the contacts between the beams so the only coupling in deformation happening between beams comes from the flow.

From Newton's third law, the force produced by the beams on the flow can be written similarly. Every beam element δS_j of beam j creates a force perpendicular to itself on the fluid

$$f_j(S_j) = \frac{1}{2} \rho d C'_D U_j^2 \sin^2 \theta_j \delta S_j. \quad (5)$$

The system has a high number of degrees of freedom, since the number of beam N is of the order of 1000 and each beam has a continuous deformation along its length. Moreover, the flow

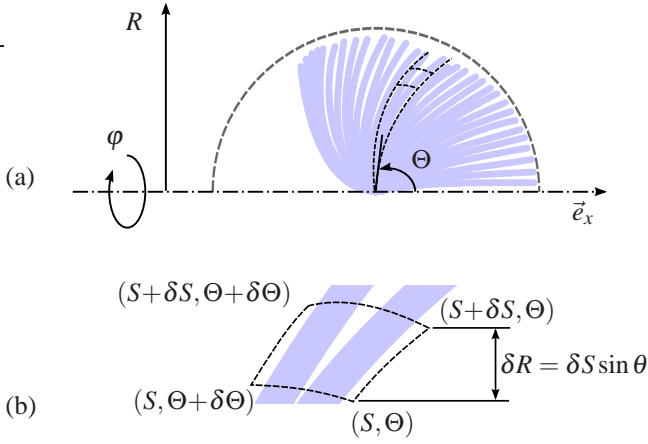


FIGURE 11: Schematic diagram of the deformation of the system (a) and detail of the section of a volume element $\delta\Omega$ of the poroelastic continuum (b).

through the multiple beams is complex. Rather than modelling all these degrees of freedom and this complexity of the flow, we use an homogenisation approach similar to Py et al. [15] and Favier et al. [16]. We consider the ball of beams as a poroelastic continuous media. Deformation of beam j , $\theta_j(S_j)$, becomes a continuous function in Θ , i.e., $\theta(S, \Theta)$. By neglecting gravity, deformation of the system can be considered axisymmetric in φ . We can thus rewrite equation 4 as

$$B \frac{\partial^3 \theta}{\partial S^3} = -\frac{1}{2} \rho C'_D [U \sin \theta]^2, \quad (6)$$

where U and θ are functions of Θ and S .

Homogenisation in space allows to model the forces that beams exert on the flow as a body force. In a volume $\delta\Omega$ of an element $\delta S \delta \Theta \delta \varphi$ as drawn in figure 11, are located $N_\Omega = N \sin(\Theta) \delta \Theta \delta \varphi / 4\pi$ beams and the body force they exert on the fluid is N_Ω times the force of one beam element from equation 5, i.e.,

$$f(S, \Theta) = \left(\frac{N}{4\pi} \sin \Theta \delta \Theta \delta \varphi \right) \left(\frac{1}{2} \rho d C'_D U^2 \sin^2 \theta \delta S \right). \quad (7)$$

In the spirit of keeping the model simple, we make the approximation that the flow is always parallel to the axis of axisymmetry of the system and neglect the transverse component, i.e. $\vec{U}_j = U_j \vec{e}_x$. It follows from this simplification that the flow can be solved with the Bernoulli equation.

For purely axial flow, the fluid in the volume $\delta\Omega$ (figure 11) flows through the surface $R \delta R \delta \varphi$, where R is the eulerian coordinate measured perpendicular to the axis of axisymmetry.

From the transformation $\delta R = \delta S \sin \theta$, we can write the loss of pressure due to drag across the volume $\delta\Omega$ as

$$\Delta P = \frac{f \sin \theta}{R \delta R \delta \varphi}. \quad (8)$$

To find the loss of velocity on a variation $\delta\Theta$, we apply Bernoulli's law, $\frac{1}{2} \rho U^2(R, \Theta) = \frac{1}{2} \rho U^2(R, \Theta + \delta\Theta) - \Delta P$:

$$U^2(R, \Theta) - U^2(R, \Theta + \delta\Theta) = -U^2(R, \Theta + \delta\Theta) \frac{N \sin \Theta \delta \Theta C'_D d \sin^2 \theta}{4\pi R}. \quad (9)$$

If the angle $\delta\Theta$ is small, equation 9 takes the form of a derivative

$$\frac{\partial U}{\partial \Theta} = U \frac{N \sin \Theta C'_D d \sin^2 \theta}{8\pi R}. \quad (10)$$

The beam located at $\Theta = \pi$ encounters an unperturbed flow U_∞ . For $\Theta < \pi$, since the deformation of the beam varies with R , the local flow velocity is a function of R .

The drag force of the entire poroelastic system is the integral over its volume of the axial component of the body force of equation 7:

$$F = \int_0^\pi \frac{N}{2} \sin \Theta \int_0^{D/2} \frac{1}{2} \rho d C'_D U^2(R, \Theta) \sin^3 \theta dS d\Theta. \quad (11)$$

To write the problem in a dimensionless way, we define the dimensionless lagrangian and eulerian coordinates, the velocity, the surface density, as well as the reconfiguration and Cauchy number

$$\begin{aligned} s &= \frac{2S}{D}, & r &= \frac{R}{D}, & \bar{U} &= \frac{U}{U_\infty}, & \eta &= \frac{2Nd}{\pi D}, \\ \mathcal{R} &= \frac{F}{\frac{1}{8} \rho \pi D^2 C'_D U_\infty^2}, & \tilde{C}_Y &= C'_D \frac{\rho D^3 U_\infty^2}{16B}, & c &= \frac{C'_D}{C_D}, \end{aligned} \quad (12)$$

where the reference drag of a rigid porous system is defined based on the *macroscopic* drag coefficient of the entire system C_D which is different from the *microscopic* drag coefficient of only one beam inside the ball C'_D , and where c is the ratio of both coefficients.

With the parameters of equations 12, equations 6, 10 and 11

are made dimensionless:

$$\frac{\partial^3 \theta}{\partial s^3} = -\widetilde{C}_Y c \bar{U}^2 \sin^2 \theta, \quad (13)$$

$$\frac{\partial \bar{U}}{\partial \Theta} = \bar{U} \frac{\eta C'_D \sin \Theta \sin^2 \theta}{16r}, \quad (14)$$

$$\mathcal{R} = \frac{\eta c}{2} \int_0^\pi \sin \Theta \int_0^1 \bar{U}^2 \sin^3 \theta \, ds \, d\Theta. \quad (15)$$

Note that we define the Cauchy number, \widetilde{C}_Y , based on the macroscopic drag coefficient of a rigid equivalent porous ball, C_D , although it is the drag coefficient of a single filament composing the ball, C'_D , that appears in equations 6 and 10. We do so because C'_D can difficultly be measured experimentally.

The dimensionless boundary conditions can be written as follows:

$$\bar{U}|_{\Theta=\pi} = 1, \quad \theta|_{s=0} = \Theta, \quad \frac{\partial \theta}{\partial s} \Big|_{s=1} = 0, \quad \frac{\partial^2 \theta}{\partial s^2} \Big|_{s=1} = 0. \quad (16)$$

To solve the system of equations 13 and 14, the deformation of the poroelastic media $\theta(s, \Theta)$ and the velocity of the fluid $\bar{U}(r, \Theta)$ are discretised in Θ over N_Θ reference beams similarly to [16]. The deformation of the upstream-most beam at $\Theta = \pi$ is solved first since it perceives an unperturbed flow velocity. Equation 13 is integrated numerically using the shooting method and the Runge Kutta algorithm. Once the deformation of this beam is known, equation 14 is solved at N_r points on r between 0 and 1 to yield the flow perceived by the second reference beam. The equation of deformation 13 is subsequently integrated numerically with Runge Kutta using an iterative scheme since the flow velocity profile is defined in eulerian coordinates and the deformation of the beam is defined in lagrangian coordinates. Once the shape of the beam is found, the loss of momentum in the flow is computed using equation 14 and the process is repeated for every reference beam and finish by solving equation 15 to find the reconfiguration number.

Note that when the poroelastic system is dense enough, i.e., when η is large, the term $(\eta C'_D \sin \Theta \delta \Theta \sin^2 \theta)/(8r)$ of equation 10 can become larger than 1 over part of r especially close to the centre of the system ($r = 0$). In this case, $u(r, \Theta)$ is set to 0 and the ‘‘additional’’ loss of momentum at this position in r is subtracted from the next position $r + \delta r$.

Also, when many equilibrium positions exist for a beam, we select the one for which the free end is the farthest downstream. No stability analysis is performed on the different positions, but we judge that this position has most chances of minimising the potential energy.

The geometry we model is slightly different from that of our experiments because we neglect to model the rigid core of the

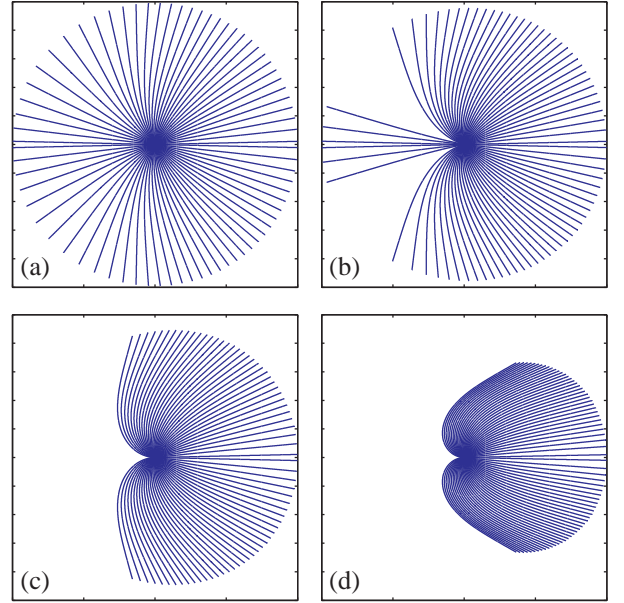


FIGURE 12: Visualisation of the modelled deformation of a poroelastic system equivalent to the first specimen subjected to a flow with $\widetilde{C}_Y = 2.8$ (a); 6.9 (b); 20.6 (c); 87.2 (d). Note that the Cauchy numbers correspond to the conditions of figure 5.

poroelastic system. Considering that all the coupling between the deformation of the beams comes from the flow and considering the simplicity of the flow model, the effect of the core is neglected. Moreover, by defining the Cauchy number based on the flexible length of the filaments ($D/2 - D_i/2$ in equation 3 and $D/2$ in equation 12), the model can be appropriately compared with the experiments.

Theoretical Results

To realise the simulations, it was necessary to provide a value for the microscopic drag coefficient C'_D which we could not measure experimentally. The model was thus used to simulate the drag of the rigid specimen tested experimentally and the value of C'_D was calibrated to make the resulting simulated macroscopic drag coefficient C_D match that measured experimentally on the rigid specimen. A value of $C'_D = 0.53$ was thus used for the remainder of the simulations.

The first and the second poroelastic specimens tested in the wind tunnel which have respectively surface densities of $\eta = 6.0$ and $\eta = 9.2$ where modelled using $N_\Theta = 120$ reference beams. The deformation of the first specimen is shown in figure 12. The deformation is qualitatively very similar to that observed in the wind tunnel in figure 5.

The reconfiguration curves predicted by the theoretical

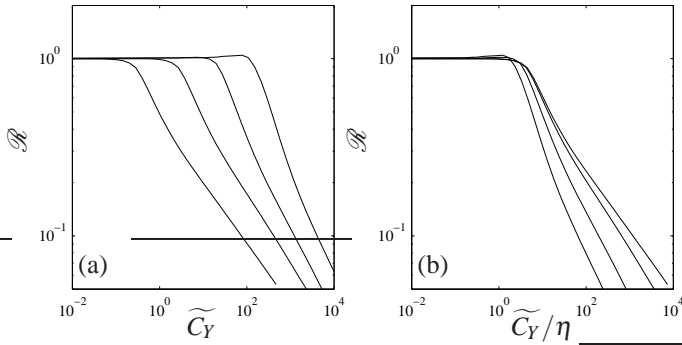


FIGURE 13: Effect of the surface density on the reconfiguration curve for poroelastic systems in function of: \widetilde{C}_Y , (a); \widetilde{C}_Y/η , (b). The curves have surface densities of $\eta = 0.1, 1, 10$ and 100 from left to right in (a) and from right to left in (b).

model of equations 13-15 with $\eta = 6.1$ and 9.2 corresponding respectively to the first (solid line) and second (dash line) specimens are shown in figure 8 for comparison with the first (\bullet) and second (\circ) experimental specimens. The general trend of the theoretical curves is the same as for the experimental points.

As the model succeeds in reproducing the experimental results in figure 8, we use it to investigate the effect of surface density on the reconfiguration. In figure 13, are plotted for a wide range of surface densities, the curves of \mathcal{R} versus \widetilde{C}_Y in (a) and versus the ratio \widetilde{C}_Y/η in (b). In (a), the curves from left to right represent systems with surface densities of $\eta = 0.1, 1, 10$ and 100 ; in (b) they go from right to left. In (a) the curves are evenly spread on the logarithmic plot, while in (b), they are made to coalesce at one point about $\widetilde{C}_Y/\eta \approx 3$. This shows that the drag reduction of the poroelastic system studied becomes significant when the Cauchy number spread over every element composing the system is effectively of order 1, i.e., $\widetilde{C}_Y/\eta \sim \mathcal{O}(1)$. The reconfiguration curve of a poroelastic system can thus be compared with that of a simple system by dividing the Cauchy number by the surface density as is done for the experimental measurements on slender filaments and plates in figure 9 (b).

The curves of figure 13 (b) coalesce at small values of \widetilde{C}_Y/η , but at high values when the deformation is large, they have different slopes. Recall that this slope is equal to half the value of the Vogel exponent \mathcal{V} . In figure 14, the value of Vogel exponent computed at $\widetilde{C}_Y c = 10^4$ is plotted in function of the surface density. On this graph, an infinitely small value of $\eta C_D'$ corresponds to the case where the beams composing the poroelastic system are thin and few. Therefore, they do not perceive the presence of their neighbors through the flow. However, when $\eta C_D'$ is large, the system has a lot of surface generating drag. At $\eta = 2 \times 10^{-4}$ in figure 14, the poroelastic system has a Vogel exponent of $\mathcal{V} = -2/3$ which corresponds to the asymptotic

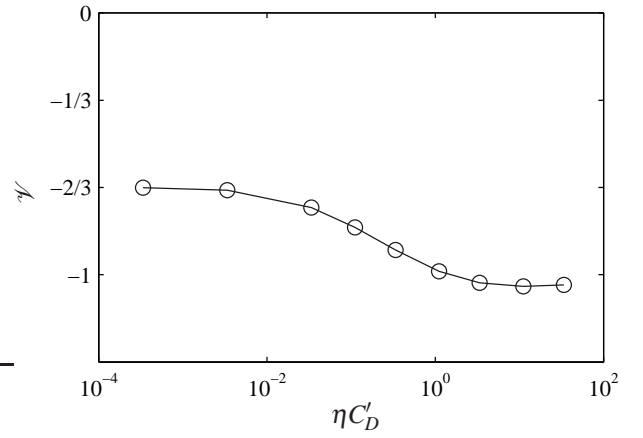


FIGURE 14: Variation of the Vogel exponent of the drag of a poroelastic system with surface density. The exponent \mathcal{V} is computed at $\widetilde{C}_Y c = 10^4$.

regime of large deformation of plates, filaments and fibres. In a range of values of $\eta C_D'$ between 2 and 34, which includes the two experimental specimens tested, the Vogel exponent is almost constant at $\mathcal{V} = -1.04$. In fact, by varying $\eta C_D'$ over two orders of magnitude between 0.3 and 30, the value of the Vogel exponent varies by less than 15%. What the model predicts is that if one of the experimental specimens had had 10 times more or 10 times less filaments, its Vogel exponent at large $\widetilde{C}_Y c$ would have been approximately the same around $\mathcal{V} \approx -1$. The scaling law of $\mathcal{V} = -1$ is robust for this poroelastic system.

CONCLUSION

By performing the first experiments on the reconfiguration of synthetic poroelastic systems, it was shown that the drag on these systems is characterised by the Cauchy number, the reconfiguration number and the surface density.

The drag of the synthetic poroelastic system studied shows particularities similar to those of real trees. As measured on branches of Loblolly Pine and American Holly by Vogel [3], the drag on the poroelastic system was measured to increase in a more pronounced way than a U^2 law because the upstream filaments realign themselves in the flow.

A model based on a conservation of momentum in the direction of the flow coupled with the large deformation Euler-Bernoulli equation of many beams allows to predict the reconfiguration of the specimens tested experimentally. The same model shows that for large enough values of surface density, the scaling law in $\mathcal{V} = -1$ at large Cauchy values is robust over a wide range of values of surface density.

On this last point, it is worth mentioning that in the literature, almost all the Vogel exponent values we found for coniferous trees are about -1 [3, 17, 18]. Moreover, these trees have

a structure that somewhat resemble that of the poroelastic system studied here. Like the balls made of filaments, coniferous trees are poroelastic structures made of lots of beams which create drag: long thin needle-like foliage. It might not be a coincidence that 4 out of 5 of the Vogel exponents we found in the literature for coniferous trees are about -1 . It would be interesting to evaluate the surface density of these species and to test specimens using the same experimental protocol used here for synthetic specimens. This would allow to understand better why there seems to be an homogeneity in the values of Vogel exponents in the literature.

ACKNOWLEDGMENT

We are thankful to Pascal Hémon for designing and building a high quality experimental set-up. We thank Silas Alben for providing us with his experimental data. We also acknowledge the financial support of the ‘Fonds québécois de la recherche sur la nature et les technologies’, École Polytechnique and the ANR program 06-BLAN=0210 ‘Chêne-Roseau’ involving INRA, INRIA and École Polytechnique.

REFERENCES

- [1] Vogel, S., 1996. *Life in Moving Fluids*, 2 revised ed. Princeton University Press, Apr.
- [2] Gardiner, B. A., and Quine, C. P., 2000. “Management of forests to reduce the risk of abiotic damage – a review with particular reference to the effects of strong winds”. *Forest Ecology and Management*, **135**(1-3), Sept., pp. 261–277.
- [3] Vogel, S., 1984. “Drag and flexibility in sessile organisms”. *American Zoologist*, **24**(1), pp. 37–44.
- [4] Vogel, S., 1989. “Drag and reconfiguration of broad leaves in high winds”. *Journal of Experimental Botany*, **40**, Aug., pp. 941–948.
- [5] Harder, D., Speck, O., Hurd, C., and Speck, T., 2004. “Reconfiguration as a prerequisite for survival in highly unstable flow-dominated habitats”. *Journal of Plant Growth Regulation*, **23**, June, pp. 98–107.
- [6] Alben, S., Shelley, M., and Zhang, J., 2002. “Drag reduction through self-similar bending of a flexible body”. *Nature*, **420**, Dec., pp. 479–481.
- [7] Alben, S., Shelley, M., and Zhang, J., 2004. “How flexibility induces streamlining in a two-dimensional flow”. *Physics of Fluids*, **16**, pp. 1694–1713.
- [8] Schouveiler, L., and Boudaoud, A., 2006. “The rolling up of sheets in a steady flow”. *Journal of Fluid Mechanics*, **563**, pp. 71–80.
- [9] Gosselin, F., 2009. “Mécanismes d’interactions fluide-structure entre écoulements et végétation”. Ph.d. thesis, École Polytechnique.
- [10] Gosselin, F., de Langre, E., and Machado-Almeida, B., 2010. “Drag reduction of flexible plates by reconfiguration”. *Journal of Fluid Mechanics*, **650**, pp. 319–342.
- [11] Cermak, J., and Isyumov, N., 1998. *Wind Tunnel Studies of Buildings and Structures*. American Society of Civil Engineers.
- [12] Chakrabarti, S., 2002. *The Theory and Practice of Hydrodynamics and Vibration*. Singapore, World Scientific.
- [13] de Langre, E., 2008. “Effects of wind on plants”. *Annual Review of Fluid Mechanics*, **40**, pp. 141–168.
- [14] Taylor, G., 1952. “Analysis of the swimming of long and narrow animals”. *Proceedings of the Royal Society of London. Series A, Mathematical and Physical Sciences*, **214**(1117), pp. 158–183.
- [15] Py, C., de Langre, E., and Moulia, B., 2006. “A frequency lock-in mechanism in the interaction between wind and crop canopies”. *Journal of Fluid Mechanics*, **568**, pp. 425–449.
- [16] Favier, J., Dauptain, A., Basso, D., and Bottaro, A., 2009. “Passive separation control using a Self-Adaptive hairy coating”. *Journal of Fluid Mechanics*, **627**(-1), pp. 451–483.
- [17] Mayhead, G., 1973. “Some drag coefficients for british forest trees derived from wind tunnel studies”. *Agricultural Meteorology*, **12**, pp. 123–130.
- [18] Rudnicki, M., Mitchell, S. J., and Novak, M. D., 2004. “Wind tunnel measurements of crown streamlining and drag relationships for three conifer species”. *Canadian Journal of Forest Research*, **34**, Mar., pp. 666–676.